Buckling of elastic columns with second-mode imperfections

P. S. Harvey Jr.[a,*], L. N. Virgin[b], M. H. Tehrani[a]

[a]*School of Civil Engineering and Environmental Science, University of Oklahoma, Norman, OK 73019, USA*
[b]*Department of Mechanical Engineering, Duke University, Durham, NC 27708, USA*

Abstract

The pin-ended, slender, Euler strut has been used as the archetypal buckling problem for many years [1]. Even though it is not conventionally imperfection-sensitive (i.e., in which the magnitude of the buckling load is compromised by the presence of imperfections), initial geometric imperfections are still important, and 3D-printing now allows a versatility in geometric prescription and accuracy previously unavailable. This paper focuses attention on Euler struts, primarily from an experimental viewpoint, in which a second mode (full sine wave) initial shape, with varying magnitude, is used to produce specimens, test them, and compare with the elementary theory.

Keywords: Euler buckling, imperfections, second mode, 3D printing, image processing

1. Introduction

Column buckling is characterized by the loss of stability of the trivial (straight) equilibrium configuration: the column finds it energetically easier to bow out sideways rather than deforming axially [2]. Buckling commonly occurs in a variety of slender structures in which there is a degree of compressive axial loading, with the relative geometric simplicity of a one-dimensional beam-column providing a natural introductory context [3–6]. Given the nominal symmetry of the system we recognize this as a pitchfork bifurcation [7, 8]. Furthermore, in contrast to imperfection-sensitive structures (like cylindrical shells) there is a degree of positive post-buckled stiffness, and it is this feature that categorizes this bifurcation as super-critical [7].

No real structure is truly symmetric, with the direction and nature of buckling depending on a number of quite subtle, apparently secondary factors like any initial geometric imperfection (lack of straightness), load eccentricity, or the presence of a small lateral load [8]. However, in bifurcation theory the role of symmetry-breaking parameters is well-recognized, and clearly the practical buckling of a column evolves in a preferred direction and in a preferred deflected shape. Although, underlying this whole process is a linear eigenvalue problem, the onset of buckling is by no means characterized by a sudden criticality, but rather the (rapidly) increasing deflection

*Corresponding author. Address: School of Civil Engineering and Environmental Science, University of Oklahoma, 202 W. Boyd St., Norman, OK 73019-1024, USA. Tel.: +1 405 325 3836

Email addresses: harvey@ou.edu (P. S. Harvey Jr.), l.virgin@duke.edu (L. N. Virgin), m.h.tehrani@ou.edu (M. H. Tehrani)

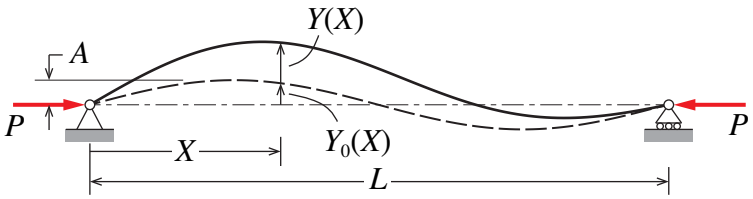

Figure 1: Pinned column with second mode imperfection.

when the axial load approaches the underlying critical load. It is the form of this deflection, and how it is related to the initial (prescribed) shape, that comprises the focus of the current paper.

In general axially-loaded structures, there are often a myriad of forms by which a *real* structure might deviate from its pristine model. For linear structures this is hardly an issue, but in the context of buckling, it is crucially important. The form of initial geometric imperfection, which might be somewhat random in nature, has often been taken as the first buckling mode shape, partly for analytic expediency, but also because the ensuing shape (eigenvector) is somewhat natural, e.g., the boundary conditions are automatically satisfied [9]. For the case of a pin-ended strut it is natural to assume the initial geometric imperfection might take the form of a Fourier series, in this case sine waves, and using the *first* buckling mode shape (a half-sine-wave) is a reasonable choice given its typical dominance, and this is confirmed by many experimental studies. But this does beg the question: if the strut has an initial shape that is *not* in the form of the first buckling mode, but say the *second* buckling mode (a full-sine-wave), how does this form, and its magnitude, influence subsequent buckling behavior? A similar question was posed in Ref. [10] using an analytic (elastica) approach. The current paper attacks this problem using carefully produced physical specimens utilizing the impressive resolution capabilities of 3D-printers [11, 12]. We also make use of the Southwell plot [13] to not only access buckling load estimates but also to extract posteriori confirmation of initial imperfections.

2. Formulation of basic problem

Fig. 1 depicts a prismatic pin-ended column of length[1] L with flexural rigidity EI under axial load P. Assuming the slope is small, the linear differential equation governing the deflected shape $Y(X)$ is given by

$$EI\,Y''(X) + PY(X) = -PY_0(X) \tag{1}$$

where $Y_0(X)$ is the initial deflection when unstrained. The initial deflection is chosen as

$$Y_0(X) = A \sin \frac{2\pi X}{L} \tag{2}$$

which corresponds to a shape in the form of the second buckling mode of the perfect column, with an initial amplitude $Y_0(L/4) = A$. The boundary conditions are $Y(0) = Y(L) = 0$.

[1]The length L used in this paper is the pin-to-pin length, as opposed to the arc length. The two are compared in Appendix A.

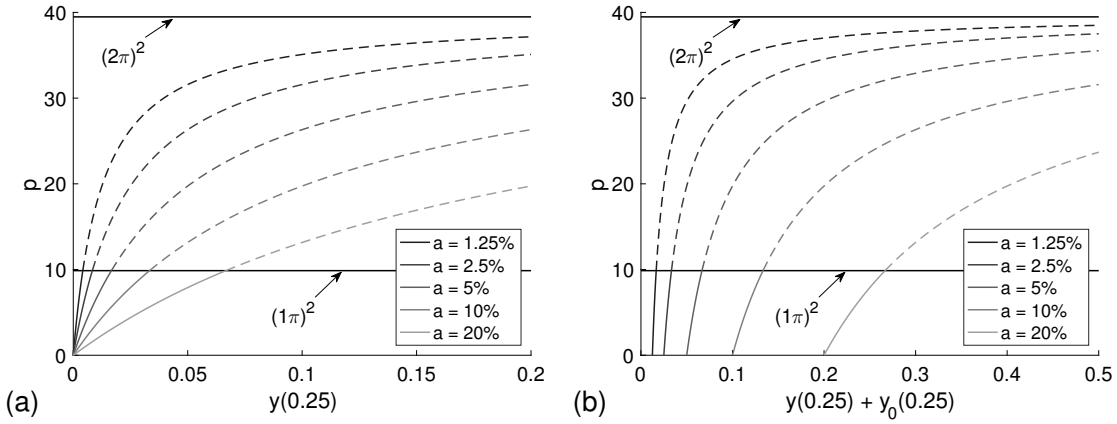

Figure 2: Theoretical load p versus lateral deflection—(a) relative deflection y and (b) total deflection $y+y_0$—at quarter point for varying imperfection amplitude a. The dashed portions are practically unreachable because the system will buckle in the first mode at $p = (1\pi)^2$ before reaching higher load.

The following nondimensional variables are defined:

$$x = X/L, \quad y = Y/L, \quad y_0 = Y_0/L, \quad a = A/L, \quad p = PL^2/EI \tag{3}$$

The nondimensional deflection of the column is given by

$$y(x) = c \sin \sqrt{p}\, x + \frac{p\, a}{(2\pi)^2 - p} \sin 2\pi x \tag{4}$$

where c is arbitrary at the buckling loads $p = (n\pi)^2$, $n = 1, 2, ...$, and $c = 0$ otherwise.

Fig. 2(a) graphically portrays Eq. (4). In particular, the second term in Eq. (4), which corresponds to the second buckling mode imperfection, is shown for varying imperfection amplitude a. These curves asymptote to the second Euler buckling load, $p = (2\pi)^2$. However, under monotonically increasing load (starting from zero), once the first Euler buckling load, $p = (1\pi)^2$, is reached, the first term in Eq. (4) is activated, and the column deforms into its first buckling mode with no further increase in load. This is apparent when a small initial imperfection in the form of the first buckling mode is included:

$$y_0(x) = \epsilon \sin \pi x + a \sin 2\pi x \tag{5}$$

in which case the deflection of the column is given by

$$y(x) = \frac{p\epsilon}{(1\pi)^2 - p} \sin \pi x + \frac{p\, a}{(2\pi)^2 - p} \sin 2\pi x \tag{6}$$

For arbitrarily small imperfection ϵ, the leading term blows up when the first Euler buckling load, $p = (1\pi)^2$, is reached. Loads greater than $(1\pi)^2$ cannot be achieved experimentally without some form of external perturbation to remote equilibria.

Fig. 2(b) shows the total deflection at quarter point, $y(0.25) + y_0(0.25)$, which has a non-zero value under zero load (i.e., the initial imperfection amplitude a). For p less than the first buckling load, the total deflection at the quarter point is given by

$$y(0.25) + y_0(0.25) = \frac{p\, a}{(2\pi)^2 - p} + a \equiv \frac{a}{1 - p/(2\pi)^2} \tag{7}$$

Experimentally, the total deflection field will be measured, and the total deflection at the quarter point will be estimated using Fourier analysis. The second (nondimensional) Fourier coefficient a_2 (see Eq. (10) below) will serve as a measure of $y(0.25) + y_0(0.25)$. Equating the expression for $y(0.25) + y_0(0.25)$ given in Eq. (7) to a_2 and rearranging terms,

$$a_2 = \frac{a}{1 - p/(2\pi^2)^2} \Rightarrow a_2 = \frac{p}{(2\pi)^2} a_2 + a \tag{8}$$

and substituting $p = PL^2/EI$,

$$a_2 = \left(\frac{(2\pi)^2 EI}{L^2}\right)^{-1} a_2 P + a \tag{9}$$

which shows that values of a_2, if plotted against $a_2 P$, will fall on a straight line [13]. This line intersects the vertical or a_2-axis at a point $(0, a)$, and its inverse slope ($(2\pi)^2 EI/L^2$) is a measure of the *second* buckling load. Application of this result to the experimental measurements will afford an estimate of the second critical buckling load, as well as an estimate of the initial imperfection amplitude a: the well-known 'Southwell plot' [13].

2.1. Finite element analysis

The foregoing theory is based on first-order stability assumptions and does not accurately capture the post-buckled behavior. In this section, some of the results from the first-order analysis are verified with a nonlinear finite element analysis. To wit, a beam with second mode initial imperfections is numerically simulated in OpenSees [14]. Twenty corotational elastic beam-column elements are used to model the beam, and the initial imperfection is seeded numerically by prescribing the node locations according to Eq. (2). Under displacement control loading using the end-shortening as the reference point, an axial load is applied up to an end shortening of 100% of the pin-to-pin length L (i.e., extremely large deflections). Fig. 3(a) shows the nondimensionalized total lateral deflection at the quarter point, which when compared to Fig. 2(b) clearly illustrates the nonlinear effects at large deflections. For all cases except $a = 20\%$, the load exceeds the second Euler buckling load, $p = (2\pi)^2$. However, such large loads are not reached in these cases (i.e., $a = 1.25\%$, 2.5%, 5%, and 10%) if the first buckling mode is seeded into the initial imperfection (Fig. 3(b)), and buckling at the first Euler buckling load, $p = (1\pi)^2$, is observed. Note that very small first-mode initial imperfections—$\epsilon/a = 5 \times 10^{-6}$ (see Eq. (5))—were used, validating the practical infeasibility of reaching the loads in excess of $p = (1\pi)^2$.

The only case that did not bifurcate at $p = (1\pi)^2$ with a first-mode imperfection of $\epsilon = 5(10^{-6})\times$ a was an initial second-mode imperfection of $a = 20\%$. Additional analyses were conducted for this case, considering larger first-mode initial imperfections: $\epsilon/a = 5 \times 10^{-3}$, 5×10^{-2}, and 5×10^{-1}. Fig. 4 shows the load versus total lateral deflection for these cases, which exhibit an increased rate of deflection when approaching the first Euler buckling load. While bifurcation-like behavior is observed, a second-mode initial imperfection of $a = 20\%$ represents an extreme initial imperfection, which falls outside of what is traditionally or reasonably thought of as a column.

Additional analyses were also conducted to determine the second-mode imperfection required to overcome the bifurcation at the first buckling load. Using the bisection method between $a = 10\%$ and 20%, it was found that a second-mode imperfection of $a = 19.2\%$ was needed to observe

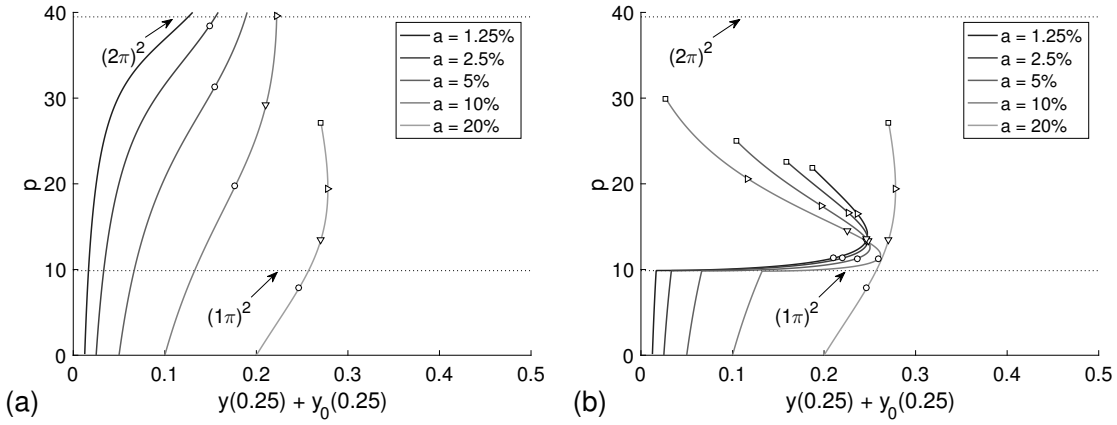

Figure 3: Finite element analysis: load p versus total lateral deflection $y + y_0$ at quarter point for varying second-mode imperfection amplitude a: (a) without and (b) with small first-mode imperfection $\epsilon = 5(10^{-6}) \times a$. The markers indicate the end shortening: 25% (○), 50% (▽), 75% (▷), and 100% (□) of the span length.

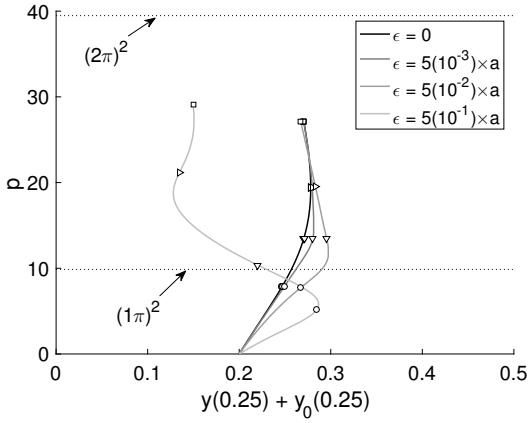

Figure 4: Finite element analysis: load p versus total lateral deflection $y + y_0$ at quarter point for varying first-mode imperfection amplitude ϵ for a second-mode imperfection of $a = 20\%$. The markers indicate the end shortening: 25% (○), 50% (▽), 75% (▷), and 100% (□) of the span length.

a bifurcation at $p = (1\pi)^2$ with a first-mode imperfection of $\epsilon = 5(10^{-6}) \times a$. Note that this corresponds to a first-mode imperfection of $9.6(10^{-7}) \times L$, which is practically infeasible to regulate.

3. Experimental Procedure

Relatively slender columns were fabricated with a consumer-grade 3D printer (Taz 6, Lulzbot, Loveland, CO). The specimens were printed out of PolyLite PLA [15], which has a published bending modulus of 3.283 ± 0.132 GPa. The "standard" (default) settings were used in the slicing software (Cura v21.08) for all specimens. The test specimens were designed to have varying initial imperfection amplitude A with a constant pin-to-pin length of 254 mm (variable arc-length). The design is shown in Fig. 5(a). Six initial imperfection amplitudes were used: $A = 3.175, 6.35, 12.7,$

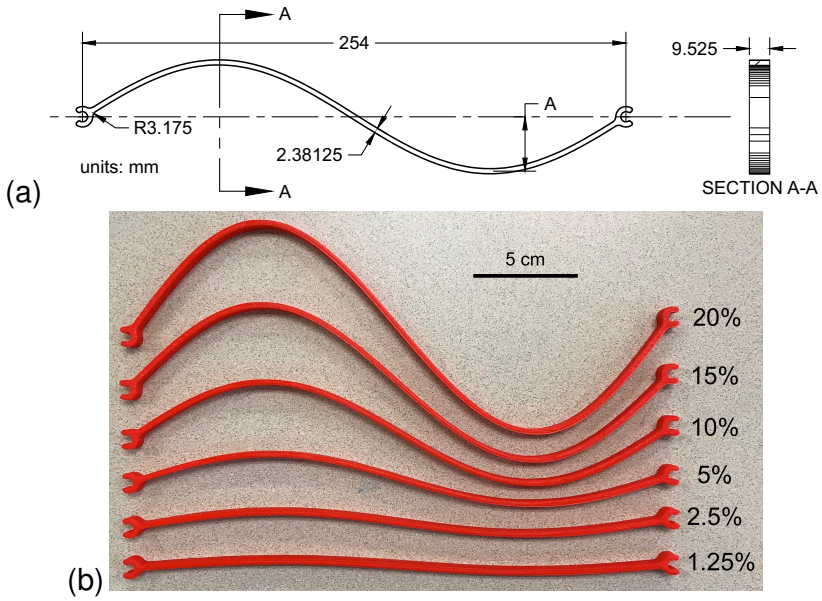

Figure 5: (a) Test specimen nominal dimensions and (b) 3D-printed specimens.

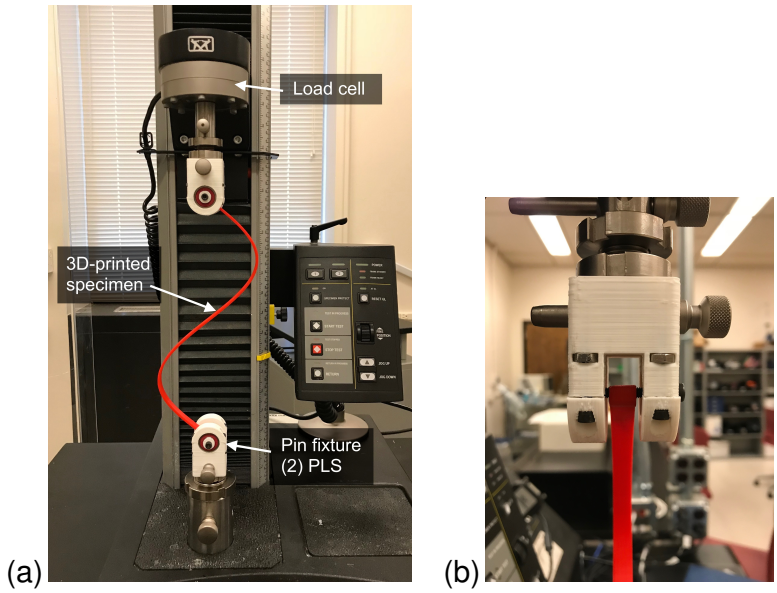

Figure 6: Photographic images of the experimental setup (a) and pin fixture (b).

25.4, 38.1, and 50.8 mm. These amplitudes correspond to non-dimensional amplitudes a = 1.25%, 2.5%, 5%, 10%, 15%, and 20%, respectively. The three 3D-printed test specimen are shown in Fig. 5(b).

The ends of the columns were designed to snap onto rotary loading pins to mimic friction-free pinned boundary conditions (see Fig. 6). Each pin fixtures was composed of a loading pin between mounted ball bearings. The pin fixtures were attached to the load heads in a Universal Testing Machine (5543, Instron, Norwood, MA) equipped with a load cell to measure the applied

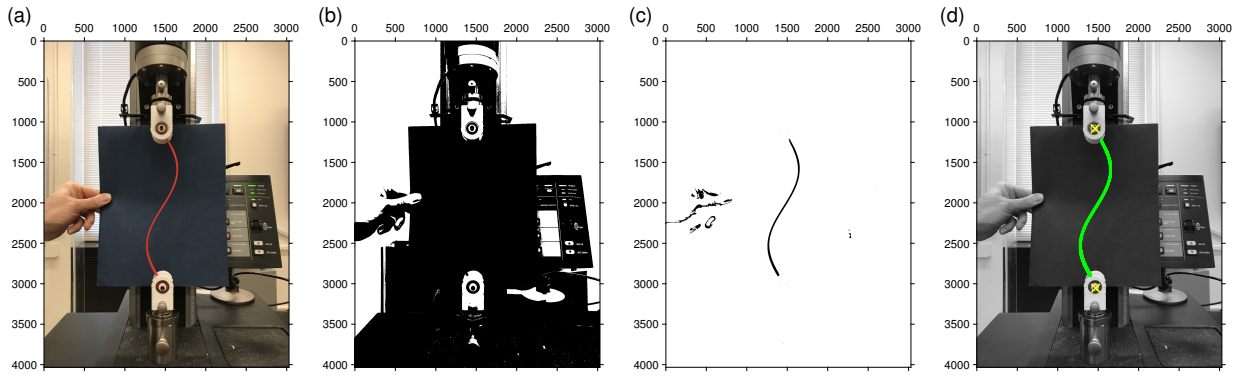

Figure 7: Image processing procedure followed to extract column shape: (a) original photo, (b) image with grey thresholding to locate pins, (c) image with grey and red thresholding to locate column, and (d) identified pins and column.

axial load. The compressive load was measured simultaneously with the end shortening during the displacement-controlled load tests. The load rate was varied (between 1 mm/min and 50 mm/min) with the maximum end shortening (0.5 mm to 100 mm); this was done because the specimens with smaller imperfections were much more sensitive to end shortening than were the specimens with larger imperfections.

In addition to measuring the end shortening, the tests were paused at approximately 1-N increments in compressive load to photograph the deflected shape. These images were processed using computer vision techniques to extract the deflected shape. Fig. 7 shows the image processing steps followed to extract the data. First, grey thresholding was used to create a binary image (Fig. 7(b)) from the original image (Fig. 7(a)). By segmenting the image, the pin locations (bolt cap head) were identified. Next, red thresholding was used to locate the red column against the blue background (see Fig. 7(a)). Because the pin fixtures are white, they passed the red thresholding, so the union of the grey and red thresholded images was taken to eliminate the pins; the resulting image with grey and red thresholding is shown in Fig. 7(c). Finally, connected component analysis (8-connectivity based) was used on the grey/red thresholded image to identify the column. Fig. 7(d) shows the identified pins and column for this particular photo.

The result of the image processing is a collection of pixel indices (I, J) of points (roughly 40,000) along the column, as well as the two pins. The points were in turn were used to estimate the deflected shape. To this end, a Fourier analysis was conducted. The pin locations were used to establish the span length (in units of pixels). The pixel indices (I, J) were then normalized by this length to arrive at a nondimensional indices (i, j). The pixel indices were also translated and rotated to establish the bottom pin as the origin with the top pin along the i (or "x") axis. Next, the Fourier coefficients a_n were fit to the pixel indices:

$$j(i) = \sum_{n=1}^{N} a_n \sin(n\pi i) \tag{10}$$

In the ordinary least squares fitting, $N = 10$ terms were retained, but the first two are of greatest interest here because they represent the terms appearing in Eq. (4).

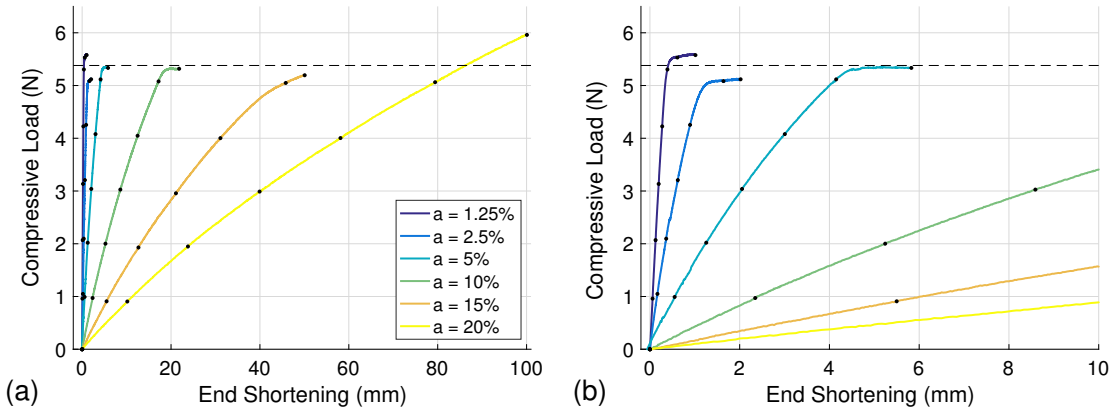

Figure 8: Experimental load versus end shortening for varying imperfection amplitude a: (a) all data and (b) expanded view in region of small end shortening. The dots indicate the load levels at which photographs were taken. The dashed line indicates the theoretical Euler buckling load.

Note that the fitting procedure assumed a linear mapping between pixel indices and physical dimensions. To try and ensure this was the case, the specimens were centered in the photos (see Fig. 7(a)) and the camera was far enough away to keep the columns/pins within the central region, occupying no more than 50% of the image height or width. Yet, there was still some degree of parallax present in the images, distorting the measurements at the extremes. In particular, the bolt cap heads that were tracked to represent the pin locations were at the very top and bottom of the region of interest, so they did not align with the end of the columns due to the image distortion. A correction was therefore required to adjust the span lengths. With this correction, better fits (i.e., containing primarily a_1 and a_2) were obtained, which are presented in the following section.

4. Results and Discussion

In Fig. 8, the compressive load P is plotted versus end shortening for the six experimental specimens. For $a = 1.25\%$ to 10%, the load-shortening curves exhibit distinct buckling behavior (end shortening rapidly increasing with small increase in compressive load) at around 5.3 N. A similar type of behavior is seen for the case $a = 15\%$, but is less pronounced. For the largest imperfection ($a = 20\%$), which is beyond the range of the simple theory, a change in the rate of increase in end shortening is not observed up to 6 N; this level of load corresponded to a 100-mm end shortening or 50% of its length.

For all but the largest imperfection used, the expected behavior is observed. That is, the column experiences progressively increasing deflection (in the second buckling mode) with load until the first buckling load is reached, at which point the column begins to deform into a combination of the first and second buckling modes (Eq. (4)). The load at which buckling occurs is relatively constant across the specimens: $P = 5.5$, 5.1, 5.3, 5.3, and 5.2 N for $a = 1.25$, 2.5, 5, 10, and 15%, respectively. These buckling loads are consistent with the theoretical value $P_1 = 5.38$ N, assuming the nominal dimensions (Fig. 1) and the PLA material properties provided by the manufacturer [15].

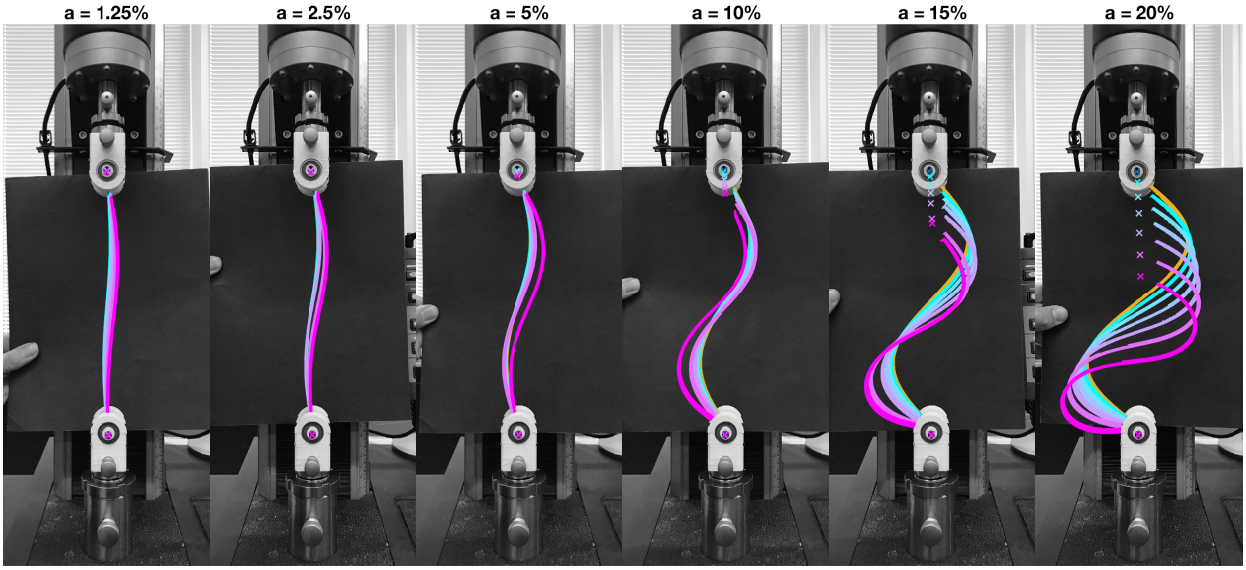

Figure 9: Equilibrium shapes for varying imperfection amplitude a. The snapshots correspond to the black dots in Fig. 8.

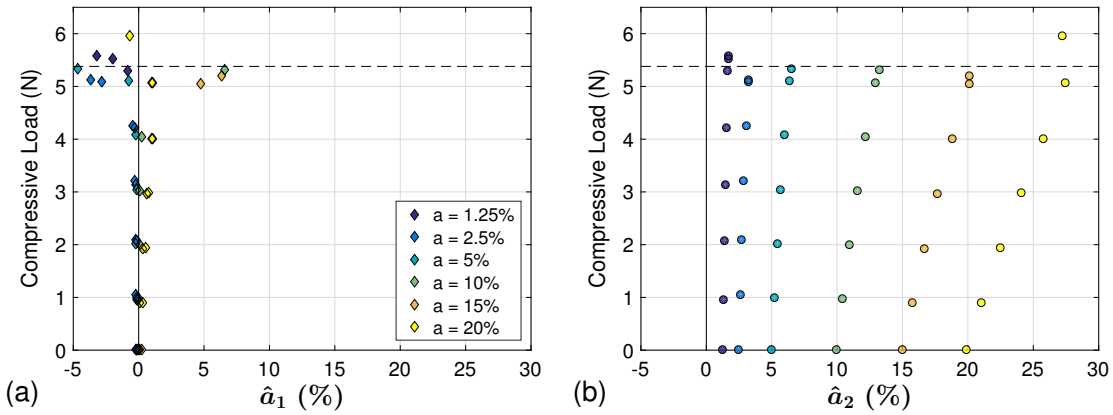

Figure 10: Fitted Fourier coefficients for shapes acquired at indicated loads points in Fig. 8 (black dots). The dashed line indicates the theoretical Euler buckling load.

The black dots in Fig. 8 correspond to the load levels at which photos were taken. Fig. 9 shows snapshots of the deflected shapes identified using image processing at each of these load levels. The progression shows that the deflected shape initially is primarily in the second buckling mode, and then a superposition of first and second buckling modes is present at larger loads/end shortening.

Fig. 9 gives a qualitative representation of the equilibrium shape, whereas Fig. 10 quantifies these shapes using a Fourier analysis. In Figs. 10(a) and 10(b), the fitted first and second Fourier coefficients, $\hat{a}_1$ and $\hat{a}_2$, respectively, are shown. Up to a compressive load of 4 N, the first Fourier coefficient $\hat{a}_1$ is very small ($< 1\%$) in all cases. The second Fourier coefficient $\hat{a}_2$ starts at roughly the initial imperfection amplitude, and then progressive increase with increasing load. The pro-

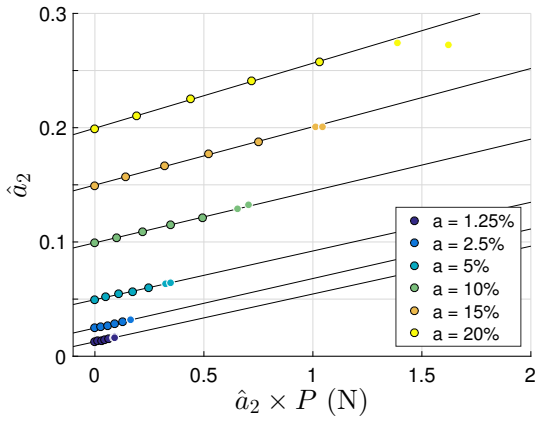

Figure 11: Southwell plot: Fitted Fourier coefficient $\hat{a}_2$ plotted against the product $\hat{a}_2 \times$ compressive load P. Observations near the Euler buckling load have been rejected in estimating the best fitting straight lines (—); such instances are distinguished by white marker edges.

gression follows the theoretical curves shown in Fig. 2(b). Once the first buckling load is reached, $\hat{a}_1$ rapidly changes (increasing to ~5%) indicating the initiation of the first buckling mode, whereas $\hat{a}_2$ stagnates. For the largest imperfection used, a similar behavior is observed (abrupt change in $\hat{a}_1$ with little change in $\hat{a}_2$), but the compressive load continues to increase. This is due less to the initiation of the first buckling mode and more to the extreme deformations in this case—there is nearly an inverted slope at the bottom pin (see $a = 20\%$ in Fig. 9), which cannot be captured with a Fourier series.

Recasting the data, Fig. 11 exhibits the relation of $\hat{a}_2$ to $\hat{a}_2 \times P$. The points for a given imperfection amplitude a fall closely on a straight line, in accordance with the relation of Eq. (9). The observations are fitted using linear least squares, and the best fitting lines are shown. Only the cases with load P below Euler buckling (i.e., up to about 4 N) are used in estimating the best fitting lines. The instances that were rejected are distinguished by the marker edge color (white). From the best fitted lines, estimates of the initial imperfection and buckling loads are given in Table 1. There is excellent agreement between the nominal imperfection amplitudes and those

Table 1: Tabulated results from Southwell plot: a = nominal imperfection amplitude, $\hat{a}$ = imperfection amplitude deduced from best-fitting line in Fig. 11, $\hat{P}_2$ = second buckling load estimated from inverse slope of best-fitting line in Fig. 11, $\hat{P}_1$ = first (critical) buckling load estimated by dividing $\hat{P}_2$ by 4, and P_1 as found from the load-end shortening data in Fig. 8.

a (%)	$\hat{a}$ (%)	$\hat{P}_2$ (N)	$\hat{P}_1$ (N)	P_1 (N)	$\hat{P}_1 \div P_1$
1.25	1.26	23.90	5.976	5.5	1.087
2.5	2.46	23.06	5.766	5.1	1.131
5	4.95	23.46	5.866	5.3	1.107
10	9.93	22.05	5.513	5.3	1.040
15	15.0	19.61	4.902	5.2	0.943
20	20.0	17.58	4.395	n/a	n/a

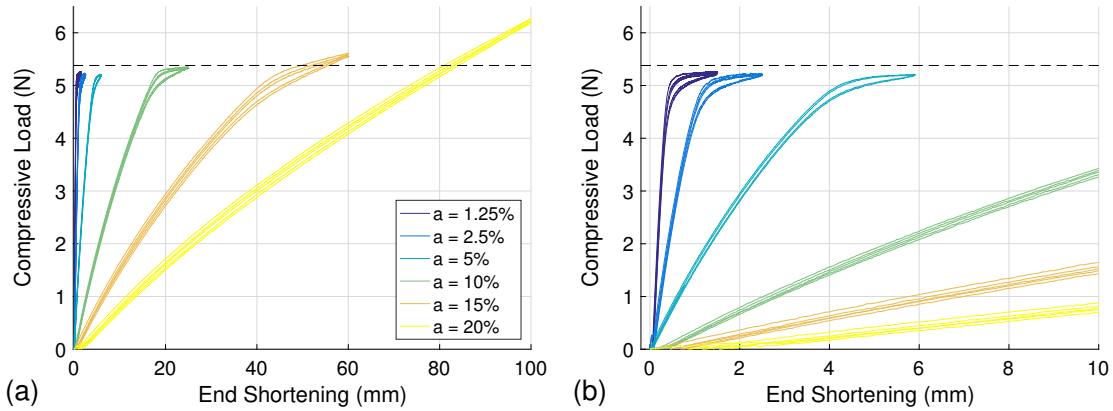

Figure 12: Experimental load versus end shortening for varying imperfection amplitude a under repeated loading/unloading: (a) all data and (b) expanded view in region of small end shortening. The dashed line indicates the theoretical Euler buckling load.

predicted using the Southwell plot. Note that, because the imperfection is in the second buckling mode, the best fitting line does not directly estimate the Euler buckling load. Instead the second buckling load is predicted (from the inverse slope), which must then be divided by 4 to predict the first (critical) buckling load, P_1. These estimated buckling loads are generally higher than those estimated from Fig. 8.

Finally, the specimens were tested under cyclic loading to check the repeatability of the results. The specimens were subjected to three loadings and two unloadings in a continuous, cyclic sequence. Fig. 12 shows the results of these tests. The load-deflection curves exhibit a little hysteresis, following different paths on loading and unloading, but the loading paths and unloading paths are self-consistent. The buckling loads in Fig. 12 are slightly lower than those observed in Fig. 8 for specimens with $a = 1.25$, 2.5, and 5%, but generally follow similar patterns. Overall, the results show an acceptable level of repeatability.

5. Concluding remarks

This paper has considered the Euler strut with imperfection that takes the form of the second buckling mode. Basic (linear) theory shows that the deflected shape follows the second buckling mode until the Euler buckling load is reached, at which point the deflected shape comprises a superposition of first and second buckling modes. Utilizing the resolution capabilities of a 3D printer, columns were fabricated with different imperfection amplitudes (from 1.25% to 20% of the pin-to-pin span length). Conventional measurements (compressive load and end shortening), as well as enhanced measurements (full-field displacements based on image processing), were made on the experimental specimens. Through a Fourier analysis, the components of the equilibrium configurations in the first and second buckling modes were extracted. The experimental data showed good agreement with the theoretical predictions, transitioning from only the second mode to both the first and second modes at the Euler buckling load.

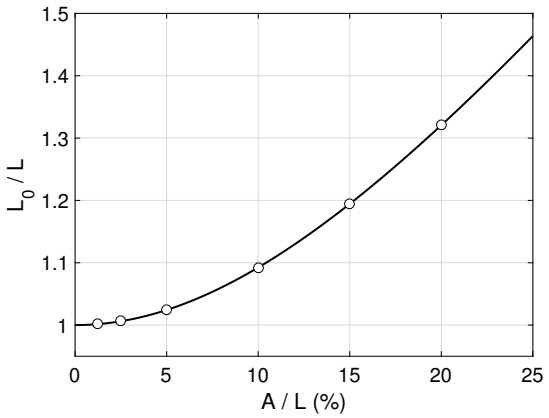

Figure A.13: Comparison of arc length L_0 to pin-to-pin length L for varying imperfection amplitude A. The circles indicate the tested cases.

Appendix A. Pin-to-pin length versus arc length

For the assumed initial imperfection (2), the arc length L_0 is given by

$$L_0 = \int_0^L \sqrt{1 + [Y_0'(X)]^2}\, dX \equiv \int_0^L \sqrt{1 + (2\pi A/L)^2 \cos^2(2\pi X/L)}\, dX \tag{A.1}$$

This is an elliptic integral that does not afford a closed-form solution. Numerically integrating this equation, the arc length for varying imperfection amplitude A is shown in Fig. A.13 in nondimensional form. For small A/L, the arc length and pin-to-pin length are approximately the same (i.e., $L_0/L \approx 1$ for $A/L < 2.5\%$). For the largest amplitude tested in this study ($A/L = 20\%$), there is roughly a 30% difference in the pin-to-pin length and the arc length. A more thorough analysis would be based on solving the elastica problem (using a shooting method for example [10]) and examining the load-deflection relation and its deviation from the harmonic form.

Acknowledgments

This material is based upon work supported by the National Science Foundation under Grant Nos. NSF-CMMI-1663376 and NSF-CMMI-1537349. This support is greatly appreciated. The authors thank Rachel C. Childers and the Stephenson School of Biomedical Engineering for providing access to the universal testing machine used in this research.

Conflict of Interest

The authors declare that they have no conflict of interest

References

[1] L. Euler, Additamentum I de curvis elasticis, methodus inveniendi lineas curvas maximi minimivi proprietate gaudentes, Bousquet, Lausanne, 1744.

[2] T. Young, Lectures on Natural Philosophy and the Mechanical Arts, Johnson, London, 1807.
[3] S. P. Timoshenko, J. M. Gere, Theory of Elastic Stability, McGraw-Hill, New York, 1961.
[4] A. Chajes, Principles of Structural Stability Theory, Prentice Hall, Englewood Cliffs, NJ, 1974.
[5] D. Brush, B. O. Almroth, Buckling of Bars, Plates and Shells, McGraw-Hill, 1975.
[6] H. G. Allen, P. S. Bulson, Background to Buckling, McGraw-Hill, New York, 1980.
[7] L. N. Virgin, Vibration of Axially Loaded Structures, Cambridge University Press, 2007.
[8] Z. P. Bazant, L. Cedolin, Stability of Structures, World Scientific Publishing, 2010.
[9] C. M. Wang, C. Y. Wang, J. Reddy, Exact Solutions for Buckling of Structural Members, CRC Press, Boca Raton, 2004.
[10] R. H. Plaut, D. A. Dillard, L. N. Virgin, Postbuckling of elastic columns with second-mode imperfections, Journal of Engineering Mechanics 132 (8) (2006) 898–901. doi:10.1061/(ASCE)0733-9399(2006)132:8(898).
[11] L. N. Virgin, Enhancing the teaching of elastic buckling using additive manufacturing, Engineering Structures 174 (2018) 338–345. doi:10.1016/j.engstruct.2018.07.059.
[12] J. H. Porter, T. M. Cain, S. L. Fox, P. S. Harvey, Jr., Influence of infill properties on flexural rigidity of 3D-printed structural members, Virtual and Physical Prototyping 14 (2) (2019) 148–159. doi:10.1080/17452759.2018.1537064.
[13] R. V. Southwell, On the analysis of experimental observations in problems of elastic instability, Proceedings of the Royal Society A 135 (1932) 601–616. doi:10.1098/rspa.1932.0055.
[14] S. Mazzoni, F. McKenna, M. H. Scott, G. L. Fenves, et al., OpenSees Command Language Manual (July 2007). URL http://opensees.berkeley.edu/OpenSees/manuals/usermanual/
[15] Polymaker, PolyLite^{TM} PLA Technical Data Sheet, Polymaker (June 2017).